Materials Science & Engineering A 908 (2024) 146779

Contents lists available at ScienceDirect

Materials Science & Engineering A

journal homepage: www.elsevier.com/locate/msea

Effect of stacking fault energy (SFE) of single crystal, equiatomic CrCoNi and Cantor alloy on creep resistance

C. Gadelmeier [a], L. Agudo Jácome [b], P. Suárez Ocaño [b], U. Glatzel [a,*]

[a] Metals and Alloys, University of Bayreuth, 95447, Bayreuth, Germany
[b] Bundesanstalt für Materialforschung und -prüfung (BAM), Materials Engineering, 12205, Berlin, Germany

ARTICLE INFO

Keywords:
Medium entropy alloy
MEA
HEA
Single crystal
CrCoNi
Creep
Stacking fault energy

ABSTRACT

Compared to mechanisms like solid solution strengthening, the stacking fault energy (SFE) should be considered as a further factor that influences the material properties. The effect of SFE of alloys or individual elements on strength and resistance can vary considerably. In the high-temperature regime above 700 °C, there are still significant gaps in the knowledge about the effect of the SFE on the mechanical properties of single-phase alloys. The effect of SFE on creep resistance of two face-entered cubic equiatomic medium and high entropy alloys, CrCoNi and CrMnFeCoNi, respectively, is evaluated to fill parts of these gaps. Using the Bridgman solidification process, the alloys were produced as single crystals and crept under vacuum at 700 °C up to 1100 °C. This work shows a significant impact of the lower SFE of CrCoNi on the creep behavior compared to the results of previous investigations of CrMnFeCoNi. The creep resistance of the former is higher over the complete temperature range. At very high temperatures, the strengthening effect of the stacking faults is significantly present. The formation of tetragonal stacking faults and extended dislocation nodes can be identified as the reason for this effect.

1. Introduction

Since about 2004, the concept of conventional alloy design evolved by expanding the degrees of freedom in the alloy composition [1,2]. Based on mixing multiple principle elements in relatively high and often equiatomic concentrations, this novel approach to concentrated solid solution alloys contrasts with the traditional alloy design [3,4]. The novel alloys are known as high entropy alloys (HEA) and medium entropy alloys (MEA) [1]. The designation HEA and MEA refer to the configurational entropy ΔS_{conf} of the solid solutions, with HEA usually consisting of five or more elements ($\Delta S_{conf} \geq 1.61$ R) and MEA of three elements ($\Delta S_{conf} = 1.10$ R) [5], with R as the molar gas constant. These new alloy systems permit the formation of unique microstructures, properties, and higher chemical complexity than alloys based on only one main component. The virtually unrestricted variety of alloying possibilities illustrates that material science of alloys has not been completely explored or even fully understood [3]. However, due to their single-phase nature, studies on HEA and MEA will lead to a more profound understanding of the overall deformation and strain hardening mechanisms. For instance, the effect of solid solution strengthening has been investigated for the face-centered cubic (FCC) $Cr_{20}Mn_{20}Fe_{20}Co_{20}Ni_{20}$ (at.%) so-called Cantor alloy and compared to pure nickel [6,7], meaning that influencing factors such as oxidation or grain size and grain boundary effects were eliminated, however the difference in stacking fault energy (SFE) was not addressed. Gadelmeier et al. [6] have shown a clear solid solution strengthening effect at 700 °C for the single-phase Cantor alloy. This effect decreases with increasing temperature and is only weakly present at 980 °C whereas at 1100 °C the effect is no longer present.

Alloying, however, does not only introduce the solid solution strengthening effect due to atomic size differences but also changes the interaction between different atomic species and thus the SFE of the solid solution. The SFE plays an important role in the mechanical properties of metals, for example, by having a strong influence on ductility and strength. Further, by only varying the chemical composition between HEA and MEA, the close-to-isolated influence of SFE on the mechanical properties, *i.e.*, the tensile properties and creep resistance, can be addressed.

The creep resistance of a material is known to depend on several factors, such as the grain structure [8,9], the stress state σ (both internal and external), the modulus of elasticity *E,* and the diffusion coefficient *D*. The relation between these quantities is given by Barett and Sherby [10]

* Corresponding author.
E-mail address: uwe.glatzel@uni-bayreuth.de (U. Glatzel).

https://doi.org/10.1016/j.msea.2024.146779
Received 1 March 2024; Received in revised form 14 May 2024; Accepted 4 June 2024
Available online 5 June 2024

in equation (1).

$$\dot{\varepsilon}_{min} = A_K \cdot \gamma_{SF}^{3.5} \cdot D \cdot \left(\frac{\sigma}{E}\right)^n \quad (1)$$

where γ_{SF} is the SFE of the alloy, A_K is a material-specific constant, n the Norton stress exponent and D is the diffusion coefficient [9,11]. Since the change in stacking fault energy is intensified by the exponent 3.5 and the change itself is way higher in comparison to D and E of all elements in consideration [12], it can be concluded that the SFE has - in our case - the strongest influence on minimum creep rate. Individual elements have different SFE, which are reflected in the SFE of an alloy depending on the content of each element. Fig. 1 shows the SFE at room temperature (RT) of different single phase FCC alloys as a function of the Ni content in comparison with pure Ni and Co.

Compared to almost all other metals, pure Ni shows the highest SFE at 120 mJ m^{-2}. The influence of Cr, Ni, and Co content on the SFE of the Cantor alloy is clearly visible. The SFE increases for alloys with much Ni and a little Cr simultaneously [8,9,20]. If there is a high Cr and Co content, the SFE decreases, which can be observed in the Equiatomic CrCoNi alloy, with an SFE of $\gamma_{SF} = 22$ mJ m^{-2} [17]. For a low SFE, *e.g.*, 10 mJ m^{-2} compared to 100 mJ m^{-2}, the recovery process in the crystal lattice is impeded by the occurrence of SF and SFE-associated defects, *e.g.,* twins. With a higher SFE, the distance between the Shockley-partial-dislocations is smaller, which results in a faster recovery of the lattice, as is observed for pure Ni. A reduction of the SFE can be achieved by adding Cr, Cu, Co or Ag to the alloy [8,9,20].

Considering the SFE and the corresponding influences of different elements on its magnitude, it is clear that the Cantor alloy, pure Ni and the equiatomic FCC CrCoNi form a suitable base of metallic materials to investigate the effect of SFE on mechanical properties of solid solutions [6,17]. Laplanche et al. [17] explored the impact of the SFE by tensile tests on the equiatomic CrCoNi compared to the Cantor alloy. They found that the separation between the Shockley-partials in CrCoNi is larger than in the Cantor alloy. Further, in CrCoNi nanotwinning is activated earlier than in the Cantor alloy as an additional deformation mechanism from RT down to liquid nitrogen temperature of −196 °C, leading to a better combination of strength and ductility. However, their study refers to polycrystalline samples at temperatures below RT. Therefore, grain-boundary effects may not be ruled out in their results, and high-temperature effects, common in high-performance alloy applications [21,22], are not considered either. Furthermore, no investigations at elevated temperatures (above 700 °C) are available so far for this alloy class. Therefore, it is unclear whether and how strong the SFE has an effect on HEA and MEA in single-phase solid solution.

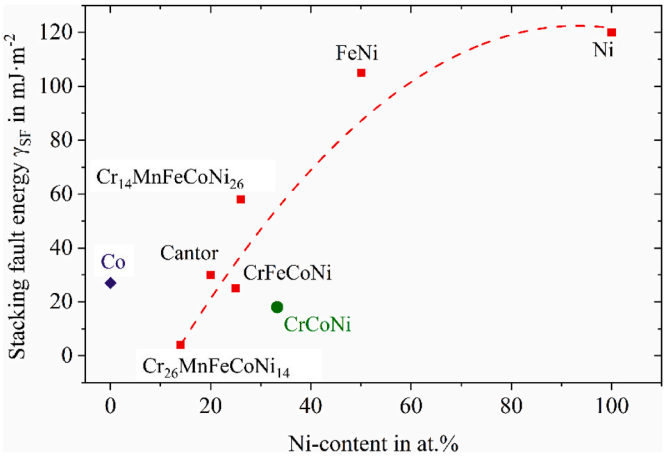

Fig. 1. *Room temperature (RT) stacking fault energies γ_{SF} [13–19] plotted over the Ni-content of single phase FCC metals. Co has a hexagonal close packed (HCP) structure as pure metal at RT. The composition of the alloys is equiatomic except for $Cr_{14}MnFeCoNi_{26}$ and $Cr_{26}MnFeCoNi_{14}$.*

In order to close this gap, our investigation is performed on the MEA CrCoNi and the HEA CrMnFeCoNi both in a single crystal (SX) and single-phase state. Therefore, diffusion processes at the grain boundaries are eliminated, thus increasing the mean free path of the dislocations. Furthermore, using an SX prevents the effect of grain boundary sliding, the latter being known to decrease the creep resistance significantly [23]. In our previous work, we reported on the isolated solid solution strengthening of the Cantor alloy in the temperature regime 700–1200 °C, and compared it to pure Ni [6]. With these data and new experiments on SX CrCoNi, presented in this paper, the influence of the stacking fault energy on the creep properties of solid solution alloys can be investigated. The creep tests on CrCoNi, as well as experiments in Ref. [6] were both performed under vacuum in order to exclude oxidation effects. Due to the different configurational entropies of the considered materials, pure Ni ($\Delta S_{conf} = 0$ R), CrCoNi ($\Delta S_{conf} = 1.10$ R), and the Cantor alloy ($\Delta S_{conf} = 1.61$ R), a possible relationship between the entropy and the material properties will also be considered [24].

2. Material and methods

2.1. Alloy manufacturing and characterization

First, the pure elements Cr, Co, and Ni (purity ≥99.95 %) were cleaned in an ultrasonic bath with ethanol and weighed in the corresponding equiatomic ratio to prepare an alloy with a total mass of 400 g. Then, eight polycrystalline master alloys (50 g each) were prepared mixing the pure metals using an arc-melting furnace (Edmund Bühler GmbH) under an argon atmosphere. These master alloys were re-melted under vacuum ($5{\cdot}10^{-2}$ Pa) in a Bridgman induction casting furnace [21,25,26] and cast into a ceramic mold with a single crystal selector. The temperature of the ceramic mold was 1520 °C which is 100 °C above the melting point of CrCoNi $T_{m\_CrCoNi} = 1417$ °C [27]. The mold was pulled down from the heating zone at a speed of 3 mm/min to solidify along the [001] orientation in the rod axis. The resulting cast rod had similar dimensions as the samples described in Ref. [6], with a length of 120 mm and a diameter of 16 mm. The manufacturing process of the SX CrCoNi was identical to the SX Cantor alloy and pure SX Ni samples [6,21,28].

Micro X-ray fluorescence (μ-XRF) investigations showed a homogeneous concentration of 33.3 ± 0.2 at.% for all elements over the whole length of the cast rod. Further, the crystal orientation in the rod axes was investigated using a SEM Zeiss Sigma 300VP with an electron backscatter diffraction (EBSD) system. The EBSD results showed no grain boundaries in the microstructure and a crystallographic orientation that deviated 28.6° from [001] ([7 4 15]) in the cast direction. The SX rod was oriented along the [001] direction using a goniometer head to align it with the tensile axis of creep specimens.

2.2. Mechanical tests

Creep specimens were prepared using wire electronic discharge machining (EDM). A sample geometry with a gage length of 5 mm between optical indicators was used, as it is reported previously [6,29]. After wire EDM, the oxidation layer was removed using a V2 etchant, and the samples were ground with a 2400 SiC emery paper.

Creep tests on the SX CrCoNi alloy were performed under vacuum at 700, 980, and 1100 °C. The same experimental setup as described in Refs. [6,21] was used. The load for the creep tests was chosen in the range of 6–120 MPa in order to compare with previous results on the Cantor alloy (leading to $\dot{\varepsilon}_{min}$ in the range of $10^{-8} - 10^{-3}$ s^{-1}) [6].

2.3. Microstructural observations

After creep deformation, chemical composition, formation of phases and sub-grains were analyzed in the CrCoNi alloy. The samples were embedded in a conductive resin, ground, polished with 1 μm diamond slurry and finally chemically polished with a colloidal SiO_2 suspension.

A scanning electron microscope (SEM) Zeiss 1540EsB Cross Beam with an energy-dispersive X-ray spectroscopy (EDS) system and a secondary electron SE detector was used for imaging.

Creeped samples of both alloys were prepared for transmission electron microscopy (TEM) in three steps. First, the complete creep samples were ground to a thickness of 100 µm, after which TEM foils with a diameter of 3 mm were punched out from the gage length area. Thus, the foil plane (110) contains the loading direction [001] in both material states. Subsequently, both sides of the foils were polished using a 3 µm and 1 µm diamond slurry, and finally thinned by Struers Tenupol-3 twin-jet electropolishing device in an electrolyte consisting of 70 vol% methanol, 20 vol% glycerol and 10 vol% perchloric acid at −25 °C and 16 V. The TEM analysis was carried out with a JEOL JEM-2200FS equipped with a field emission gun (FEG) source working with an acceleration voltage of 200 kV. Bright field (BF) and high angle annular (HAA) DF micrographs were acquired in the scanning mode (STEM) for dislocation analysis and atomic number contrast, respectively. Several overview images and further detailed images were taken from each sample. Finally, three detailed images (same region size) of each alloy were used to determine the dislocation density. The mean value including statistical deviation was calculated from the evaluation. Individual areas in the detailed images (with dislocation accumulations or a low number of dislocations) were also investigated and the dislocation density was determined.

3. Results and discussion

3.1. Creep experiments

Fig. 2a shows examples of tensile creep curves of the SX CrCoNi at 700 °C (under vacuum), one with incremental load steps between 60 and 100 MPa over time and one at a constant load of 120 MPa. Both experiments were interrupted (marked with open circles) after 451 h and 43 h, with 4.0 % and 3.7 % total strain, respectively. As seen in Fig. 2b, the incremental load steps of the first creep test occurred whenever the minimum creep rate was reached, applying the same procedure for the SX Cantor alloy experiments as in Ref. [6]. The second creep test, with a constant load of 120 MPa, was interrupted after reaching the minimum creep rate to preserve the defect structure for subsequent TEM analysis. The samples were cooled down under load after the heat source was turned off.

The experimental response of the creep tests of SX CrCoNi at 980 °C and 1100 °C is very similar to the response of the 700 °C experiments. Here, the applied load was between 12 and 40 MPa at 980 °C [21], and between 6 and 15 MPa at 1100 °C. These tests were performed until rupture. The applied creep load range of 6–120 MPa for all SX CrCoNi creep tests is comparable to the experimental conditions of the SX Cantor alloy in Ref. [6], which load range was 2–125 MPa.

Using the double logarithmic-scaled Norton-Plot, the minimum creep rates versus load (assuming $\dot{\varepsilon}_{min} \approx \sigma^n$), taken from the creep test results, are presented in Fig. 3 for the SX CrCoNi and SX Cantor alloys [6] for all temperatures. The determined values are also listed in Table 1 for comparison. At a first glance, a strong difference in creep resistance is observed between the two materials, represented by the marked green areas. More precisely, for all investigated temperatures a lower minimum creep rate is found for the SX CrCoNi alloy. Thus, the SX CrCoNi creep resistance is significantly higher than for SX Cantor alloy. The difference of <5 % in the melting temperatures of both alloys is insufficient to explain the strong differences in minimum creep rate. With a fit of Equation (2), the stress exponent n is calculated. With n between 4.3 and 6.8 for all investigated temperatures, it can be said that they have similar values of n, which points towards the similar creep mechanisms, namely, dislocation creep-controlled.

Table 2 lists the load σ to reach a steady-state strain rate of $1{\cdot}10^{-7}$ s^{-1} at 700 °C, 980 °C, and 1100 °C for the two SX solid solutions (SX CrCoNi and SX Cantor alloy), and for the pure SX Ni [6]. The CrCoNi shows the highest, and pure Ni the lowest stress values, whereas the values for Cantor alloy lie in-between. To ensure better comparability, on the right side of Table 2 the relation between the three materials is given as a relative factor of the load values on the left side (SX Cantor alloy vs. SX Ni, SX CrCoNi vs. SX Ni, SX CrCoNi vs. SX Cantor alloy). Increasing the temperature from 700 °C to 1100 °C leads to a decrease of these factors,

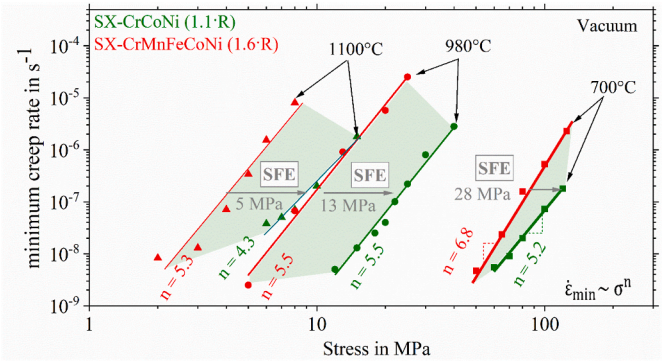

Fig. 3. Double logarithmic plot of minimum creep rate versus stress for the SX CrCoCNi compared to the SX Cantor alloy at 700, 980, and 1100 °C under vacuum. The melting points of both alloys with Tm_CrCoNi = 1417 °C and Tm_CrMnFeCoNi = 1340 °C differ only slightly by less than 5 % [27,30].

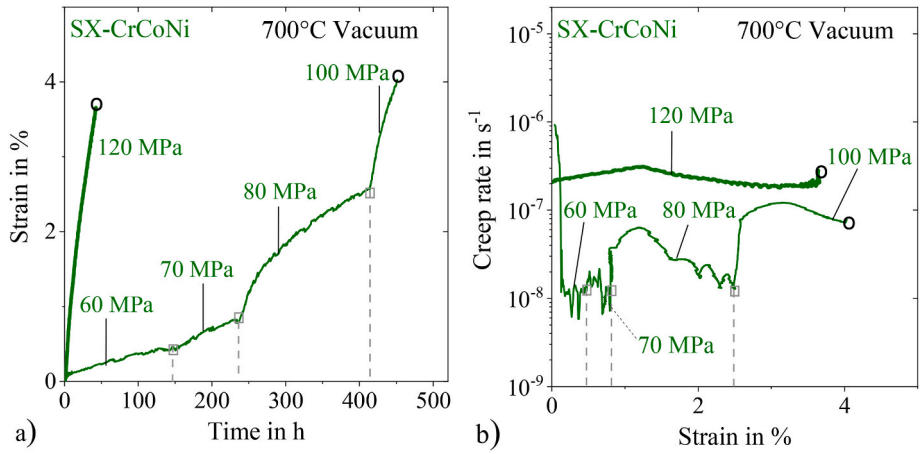

Fig. 2. a) Strain vs. time and b) creep rate vs. strain diagrams for creep tests at 700 °C (in vacuum) of the single crystalline CrCoNi alloy. Both tests were interrupted and cooled down under load. One sample was tested with a stepwise load increase from 60 to 100 MPa and one, at a constant load of 120 MPa.

Table 1
Minimum creep rates and stress exponents for the creep tests of SX CrCoNi compared with results of SX Cantor alloy [6] at different loads and temperatures under vacuum.

	$\log_{10}\dot{\varepsilon}_{min}$ in s^{-1}					
Material	SX CrCoNi			SX Cantor alloy [6]		
Temperature in °C	700	980	1100	700	980	1100
Load in MPa						
2						−8.1
3						−7.9
4						−7.1
5						−6.5
6			−7.4			−5.8
7			−7.3			
8			−7.2		−7.2	−5.1
10			−6.7			
12		−8.3				
13					−6.0	
15		−7.9	−5.7			
18		−7.6				
20		−7.4			−5.2	
22		−7.0				
25		−6.7			−4.6	
30		−6.1				
40		−5.6				
50				−8.3		
60	−8.0					
65				−7.6		
70	−7.9					
80	−7.7			−6.8		
100	−7.1			−6.3		
120	−6.7					
125				−5.6		
Norton exp. n	5.2	5.5	4.3	6.8	5.5	5.3

except for the SX CrCoNi vs. SX Cantor alloy relation at 700 °C. Between SX Cantor alloy and pure SX Ni, the factor decreases from 4.5 to 1.0, whereas between SX CrCoNi and SX Ni this value changes from 6.1 to 2.2. Therefore, to reach the minimum creep rate of SX Ni, a higher stress must be applied on both SX Cantor alloy and SX CrCoNi at all temperatures. This behavior is attributed to the solid solution strengthening effect [6], which is absent in pure SX Ni. The difference in the minimum creep rates between SX Cantor alloy and SX Ni decreases by increasing temperatures from 700 to 1100 °C, and the solid solution strengthening effect is only very weakly present at 980 °C with a factor of 1.03 in stress relation [6,21].

The higher difference in required stresses between the SX CrCoNi alloy and pure SX Ni (see Table 2) causes the variance between SX CrCoNi and SX Cantor alloy, with the factors showing a slight increase in stress ratio from 1.4 over 2.4 to 2.1 (for 700 °C, 980 °C and 1100 °C). This dissimilarity cannot be explained by an entropy effect.

The relative difference of the atomic radii δ in an alloy is calculated for both solid solutions with the radius r_i and concentration c_i of each element [31] using Equation (2).

$$\delta = \sqrt{\sum_{i=1}^{s} c_i \cdot \left(1 - \frac{r_i}{\bar{r}}\right)^2} \quad \text{with } \bar{r} = \sum_{i=1}^{s} c_i \cdot r_i \tag{2}$$

The values are 3.6 % for the SX Cantor alloy and 1.6 % for the SX CrCoNi alloy. Therefore, the Cantor alloy should show an increased creep resistance in comparison to SX CrCoNi, which is not reflected in our results.

According to Equation (1) the lower SFE of SX CrCoNi (γ_{SF} = 22 mJ m^{-2} at RT) is shown to be an advantage for the creep resistance against SX Cantor alloy (γ_{SF} = 30 mJ m^{-2} at RT) [17]. Therefore, the higher creep resistance of SX CrCoNi can be explained by a reduction in SFE [17]. While the difference in room temperature SFE of 8 mJ m^{-2} may seem small, the microstructural observations made in Section 3.2 imply a more pronounced difference in SFE present at 700 °C. Furthermore, no other influence factors can explain the significantly better creep properties of CrCoNi. The higher amount of 33.3 at.% Cr and Co in SX CrCoNi compared to 20 at.% in SX Cantor alloy can be identified as the main reason for the better properties. It has been proven that these two elements reduce the SFE of an alloy [9]. In addition, a higher amount of Cr and Co, or the elimination of Fe and Mn, leads to better mechanical properties [17,32].

3.2. Microstructural investigations

Even for the long creep test times (t > 400 h), it can be stated for both the SX CrCoNi and SX Cantor alloy, that no new phases grow (based on our EDX analysis). This is in agreement with Otto et al. [33], where decompositions occurred only after way longer exposure times (more than 10,000 h) in polycrystalline samples. Further, the chemical composition of all tested creep samples remains homogeneous and equiatomic over the whole sample.

For both SX CrCoNi and SX Cantor alloy, one interrupted creep sample each was analyzed using STEM. Table 3 lists the corresponding creep parameters, together with the determined minimum creep rates and the plastic strains at which the tests were interrupted. Both samples were tested at a temperature of 700 °C and interrupted (cooled down under load) at an identical minimum creep rate of $2{\cdot}10^{-7}$ s^{-1}. The stress level of SX CrCoNi was 1.5 times higher in comparison to SX Cantor alloy.

Fig. 4 shows BF-STEM images of the SX Cantor alloy sample after creep testing at 700 °C and 80 MPa, and the corresponding selected area diffraction pattern (SADP) indexed along the zone axis Z = [110] (see Fig. 4a). The orientation from the SADP was used to draw an identically oriented schematic lattice cell next to it, where the main directions and the traces of two edge-on {111} are labeled. The overview image (Fig. 4b) shows an inhomogeneous dislocation density. Beside dislocation-free areas (blue regions, each area with 0.8 μm^2), dislocation forests are observed (Fig. 4c), which limit the mobility of gliding dislocations [11]. Local dislocation clusters are also identified (see Fig. 4d), resulting from the pile-up of long dislocations, which are found close to

Table 3
Test parameters for the interrupted creep tests of SX CrCoNi and SX Cantor alloy (cooling under load).

	SX CrCoNi	SX Cantor alloy
temperature in °C	700	700
stress σ in MPa	120	80
minimum creep rate $\dot{\varepsilon}_{min}$ in 10^{-7} s^{-1}	2	2
strain ε in%	3.8	4.9
time in h	43	65

Table 2
Required stress to reach a steady-state strain rate of $1{\cdot}10^{-7}$ s^{-1} for SX Ni, SX CrCoNi and SX Cantor alloy. Determined factor between the three SX materials with Ni [6], CrCoNi and Cantor alloy [6] at 700, 980 and 1100 °C.

Temperature T in °C	Load σ in MPa to reach $\dot{\varepsilon}_{min}$ = $1{\cdot}10^{-7}$ s^{-1}			Temperature T in °C	Factors between the SX materials		
	700	980	1100		700	980	1100
SX Ni	17.8	7.2	3.5	**Cantor alloy vs. Ni**	4.5	1.3	1.0
SX CrCoNi	108.3	22.0	8.1	**CrCoNi vs. Ni**	6.1	3.1	2.2
SX Cantor	80.3	9.1	3.6	**CrCoNi vs. Cantor**	1.4	2.4	2.1

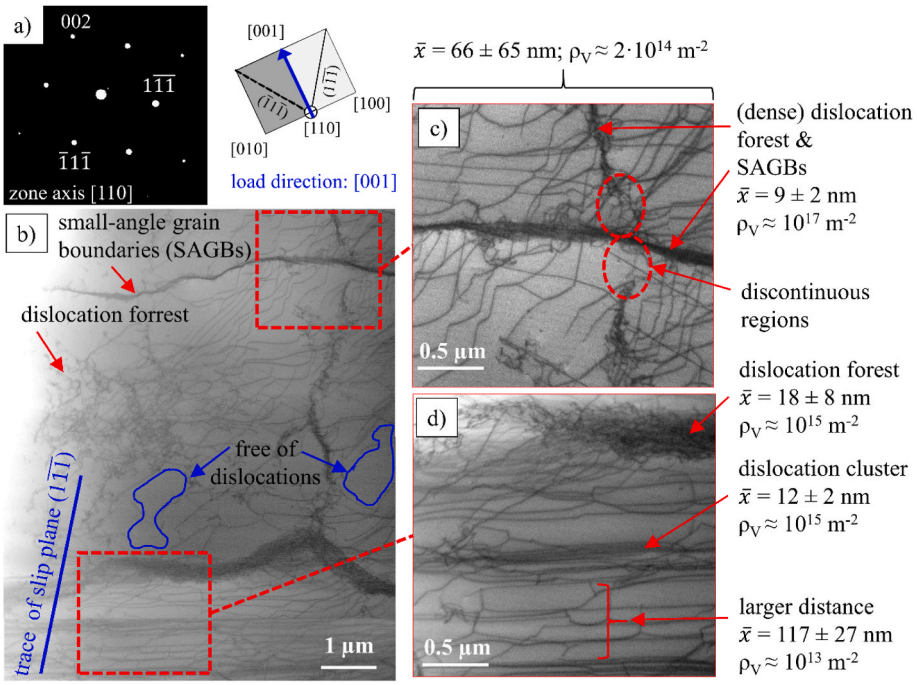

Fig. 4. BF STEM images of a Cantor alloy creep sample, interrupted after reaching the minimum strain rate at 700 °C and 80 MPa: a) selected area diffraction pattern (SADP) along the zone axis [110] and accordingly oriented schematic lattice cube; b) overview image; c) and d) detail images with long dislocations and small-angle grain boundaries.

small angle grain boundaries (SAGB, see Fig. 4b and c). The SAGB indicated in Fig. 4 was identified by acquiring convergent-beam electron diffraction (CBED) patterns on both sides of the boundary and identifying a small but clear misorientation of ≈1°. While these zone-axis images alone are not conclusive of what type of substructure the dislocations clusters form, it is reasonable to consider the dislocation alignment and their closeness to SAGB as indicative of them evolving to form the clusters. The presence of clusters with long and straight dislocation segments that are contained in the thin foil indicate glide planes where short-range order (SRO) has been broken and has led to localized preferred glide even at this temperature, as also found for other Ni-containing solid solutions [34]. This is also observed at RT and lower temperatures for the Cantor alloy [35] and may partly explain serrations observed in the creep curves presented previously [6].

Fig. 4c shows that the progress of small-angle grain boundaries is partly discontinuous for the Cantor alloy. What seems to be an early stage of dislocation rearrangement (polygonization) of a vertical forest dislocation wall is probably interrupted by a more advanced stage of SAGB buildup going horizontally, where some forest dislocations of the vertical wall may have been annihilated. With an averaged distance $\bar{x} \approx$ 66 nm between dislocations, the dislocation density [36] is $\approx 10^{14}$ m^{-2} for the Cantor alloy. The dislocation density of the small-angle grain boundaries is $\approx 10^{17}$ m^{-2}. However, the dislocation density in areas among these structures is reduced (see Fig. 4d). Dislocation forests and clusters show a dislocation density of $\approx 10^{15}$ m^{-2}, whereas areas with a larger dislocation distance of 117 nm have a dislocation density of $\approx 7 \cdot 10^{13}$ m^{-2}. No stacking faults are observed for the Cantor alloy throughout the TEM specimen. Overall, the dislocation structure in Fig. 4b can be interpreted as an ongoing process of subgrain boundary formation in the steady state creep stage where a dynamic equilibrium is reached between the dislocation forests and SAGB, which act as strain-hardening obstacles, and polygonization and annihilation as recovery processes.

In Fig. 5, anaglyphs at low (Fig. 5a) and high (Fig. 5b) magnification of a second region in the crept SX Cantor alloy sample allow for a qualitative three-dimensional (3D) impression of some of the dislocation

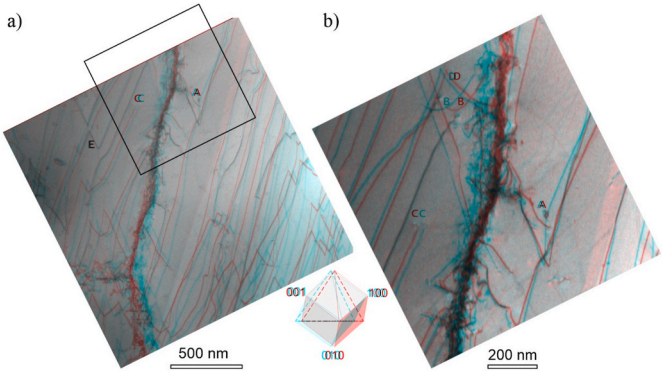

Fig. 5. *3D anaglyphs of the dislocation substructure in a Cantor alloy creep sample, interrupted after reaching the minimum strain rate at 700 °C and* 80 MPa. *(a) Large field of view. (b) Higher magnification.* $\mathbf{g} = (1\bar{1}1)$. *The schematic lattice cube in the bottom middle shows the overall orientation is found between [121] and [110].*

processes mentioned above. Thus, the small loop marked with an "A" in Fig. 5a and b nucleated on the $(11\bar{1})$ plane (cf. schematic 3D cube in the center of Fig. 5). Such a loop bows out under the effect of the externally applied effective shear stress, such that part of it looks like the arc marked "B" in Fig. 5b. While the latter seems to be strongly acted upon by the evolving dense dislocation network in the middle, long straight parallel segments such as that marked "C" seem to align on one trace of the $(11\bar{1})$ plane, thus probably starting a dislocation cluster. The "C" dislocation is thus the top-most of at least three dislocations contained in this region of the TEM foil, with the next row of two dislocations starting towards the left corner of Fig. 5b. These long segments adopt a line direction close to $[1\bar{1}0]$, which is contained in the TEM-foil plane (cf. Section 2.3), thus explaining their long character. A similar situation is displayed by the dislocation marked "D" in Fig. 5b, which bows out on the $(\bar{1}11)$ plane ahead of dislocation "B". However, dislocation "D" has met the straight $[1\bar{1}0]$ dislocation close to the bottom of the foil, the third

in the row starting with "C" at the top and is also pinned on the right side by the dense dislocation network. A considerable number of other straight segments parallel to $[01\bar{1}]$ could be associated to glide on $(\bar{1}11)$, then leaving jogs such as that marked by "E". Many other dislocations parallel to $[01\bar{1}]$, which are not left-over jogs are found, but these are considerably shorter than the $[1\bar{1}0]$ segments, as the former is not contained in the foil plane.

Long and straight dislocation segments are indicative of slow motion, which is due to reduced drag forces caused by the HEA lattice. However, difference to RT and low-temperature configurations, the dislocations found here do not have serrations characteristic of jerky motion, which are due to the high temperature mobility that allows the dislocations to minimize their line energy by proper short-range diffusion. Indeed, the activation energies for diffusion of the elements in the Cantor alloy as determined by Tsai et al. [37] are very similar, which should allow for a homogeneous redistribution of elements around dislocations.

Fig. 6 shows BF-STEM images of the interrupted SX CrCoNi sample after creep testing at 700 °C and 120 MPa. Similar to the SX Cantor alloy, the corresponding selected area diffraction pattern (SADP) was indexed along the zone axis $Z = [110]$ (see Fig. 6a), which practically coincides with the foil plane normal. At a first glance (Fig. 6b), elongated and structured dislocation network cells cover the entire sample. The cell walls tend to be parallel to [001], which corresponds to the loading direction. This contrasts the results for the SX Cantor alloy, where such a pattern is absent. Based on Fig. 6c, an averaged dislocation density $\rho_V \sim 10^{14}$ m^{-2} is estimated for SX CrCoNi. Comparable to SX Cantor alloy, SX CrCoNi is divided into areas with a very low dislocation density ($\approx 10^{13}$ m^{-2}, nearly free of dislocations, yellow frame in Fig. 6c) and areas with a high density ($\approx 10^{16}$ m^{-2}, white frame). A higher density refers to dislocation clusters oriented along [001] (loading direction) as well as others often orthogonally cross-linked to it. Fig. 6c and d shows Orowan and small freshly nucleated loops (10–220 nm in size) close to the clustered dislocations. Also, blue (Figure 6*c*) and orange (Figure 6*d*) arrows respectively mark the traces of thin segments contained within $(1\bar{1}\bar{1})$ and $(\bar{1}1\bar{1})$ (refer to the schematic lattice cell in Fig. 6a), indicative of localized glide on a few parallel planes. The latter, as with the SX Cantor alloy, may be associated to preferred glide along discrete planes where SRO has been broken. Together with the Orowan loops at different inclinations, these traces suggest glide on all four {111} planes due to similar Schmid factors that arise from the highly symmetric loading along [001].

In contrast to SX Cantor alloy, CrCoNi contains a larger number of SF, which are located preferably in the areas of dislocation clusters (see Fig. 6c and d). Fig. 7 shows details of the SF in the crept SX CrCoNi alloy. The observed SF can be categorized into two main types: 1) several extended dislocation nodes with planar SF [38] are observed in Fig. 7a; 2) further and most frequently, the SF also appear as the faces of small tetrahedral structures (Fig. 7b). In Fig. 7c–a region is shown in which the extended dislocation nodes, some small tetrahedra (dotted region), small loops, and many perfect dislocation lines contained in different {111} planes (see traces in Fig. 6a), are all present.

The large number of extended dislocation nodes alone fingerprints its low SFE even at such an elevated temperature as 700 °C. Similar dislocation nodes were commonly observed by Laplanche et al. [17] in tensile tests at liquid nitrogen temperature, −196 °C, and RT for the CrCoNi and the Cantor alloy. In the present work, no SF are observed in the SX Cantor alloy at 700 °C, indicating a strong increase in SFE with temperature, which in turn is reflected by the lower applied stress required to reach the same strain rate. The Burgers vectors of dislocations that describe the nodes are shown schematically in Fig. 7d according to Refs. [38,39], where SF appear when glide dislocations react and split into Shockley-partial dislocations [40]. In Fig. 7d, perfect dislocations with Burgers vectors (in Thomson's notation) $\boldsymbol{BA} = a/2\ [\bar{1}\ 10]$, $\boldsymbol{CA} = a/2\ [01\ \bar{1}]$ and $\boldsymbol{BC} = a/2\ [\bar{1}\ 01]$ (black vectors) split into partials with Burgers vectors $\boldsymbol{B\delta} = a/6\ [\bar{2}\ 11]$, $\boldsymbol{\delta A} = a/2\ [\bar{1}\ 2\bar{1}]$ and $\boldsymbol{\delta C} = a/2\ [\bar{1}\bar{1}\ 2]$.

The appearance of extended nodes in TEM images is exploited since 1970 [41] to accurately measure the SFE by assuming a stable state of the node, in which the line tension and SFE repel and are equal to each other. However, the extended nodes in Fig. 7a reveal several non-equilibrium features: there are many nodes with different sizes close to each other, which are asymmetric (see red arrows), and may even have abrupt cusps on the partial dislocation lines (see blue arrow). Perfect dislocations often present constrictions (green arrows), which

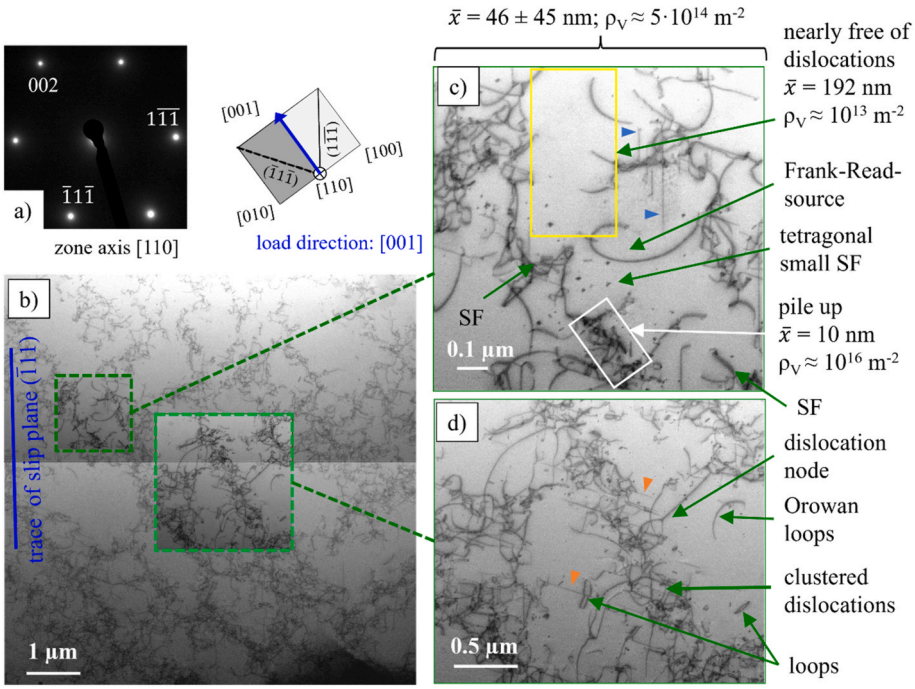

Fig. 6. BF STEM images of a SX CrCoNi creep sample, interrupted after reaching the minimum strain at 700 °C and 120 MPa: a) SADP along the zone axis [110] and accordingly oriented schematic lattice cube, b) overview image of the dislocation structure; c) and d) detail images of the characteristic dislocation configurations.

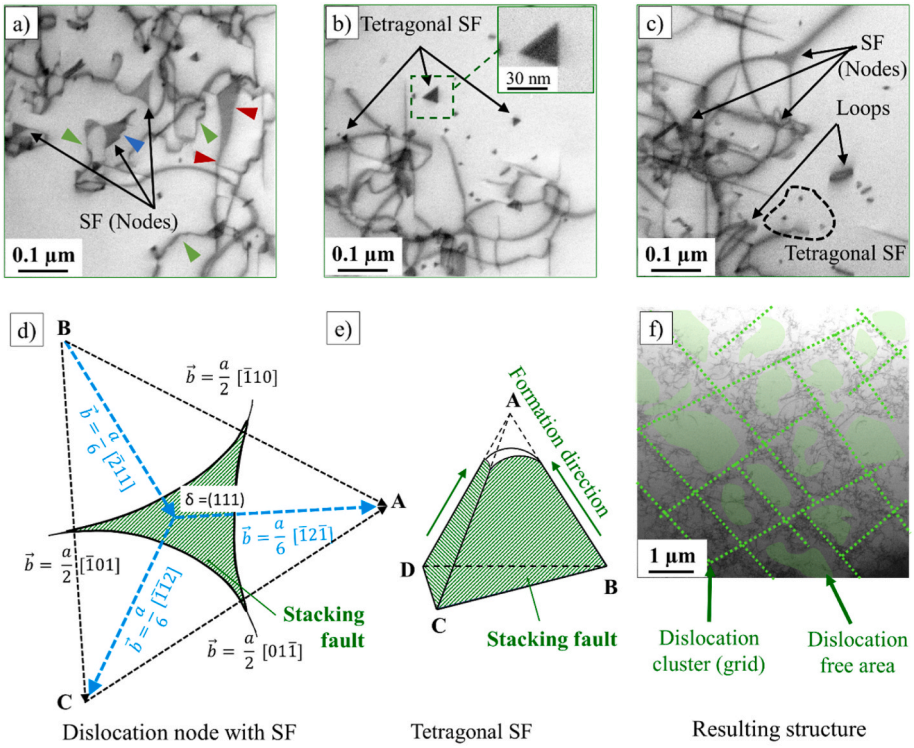

Fig. 7. *Observed SF in the SX CrCoNi alloy: a) extended dislocation nodes with SF, b) tetrahedral SF and c) combined nodes, tetrahedra, loops and perfect dislocations. Schematic illustration of the SF in the SX CrCoNi alloy: d) splitting of glide dislocations into Shockley-partial dislocations in an extended dislocation node containing SF in (1$\bar{1}$1) plane* [38,39]*; e) formation of a tetrahedral SF* [38,43]*. f) Low-mag. STEM-BF image of the heterogeneous dislocation substructure in SX CrCoNi.*

evidence short range forces acting upon them [41]. The latter may be indicative of stronger solute interactions for CrCoNi than for the Cantor alloy. While the relative difference as measured by Equation (2) yields a larger value for the SX Cantor alloy, the presence of SFs induced by Cr and Co may lead to a local redistribution of such elements around them or even change their relative atomic radii. In that case, one could speculate that for the less entropic CrCoNi one of these atoms could acquire a more significant radius difference to the others and act as solute diffusing to either side of the edge component of dislocations, i.e., the Suzuki effect [42]. As in the case of SRO disruption, such an environment could lead to dynamic strain aging, which in turn could be partly associated to serrations observed in the corresponding creep curve in Fig. 2b. While this scenario cannot be discarded, such interpretations must be cautious, as the equipment used is known to show such instabilities in the low strain-rate regimes. In passing, be noted that dynamic strain aging and its associated solute drag has been suggested by He et al. [12] to occur in the Cantor alloy at temperatures >750 °C for creep regimes with Norton exponents $n \approx 3$ and not for dislocation-climb mediated regimes of $n \geq 5$, which is the case here.

An attempt to measure the SFE on the extended nodes in Fig. 7a [43], while inaccurate due to the aforementioned asymmetry and size distribution, reveals a minimum cutoff value of 27 mJ m^{-2}. A maximum cutoff reference can be the SFE for pure Cu (≈55 mJ m^{-2}), where the extended node method can barely be applied since the separation between partial dislocations reaches the resolution of the method.

Fig. 7b shows tetrahedral SF (≈5–30 nm in edge length), formed within the dislocation cluster zones. Comparable structures have been observed in gold, a low-SFE material, quenched from high temperatures [43]. Fig. 7e schematically shows a SF tetrahedron according to Refs. [38,43]. The tetrahedral defects are explained by a collapse of vacancies that forms a Frank-type SF on a {111} plane, ($\boldsymbol{b}$ = a/3<111>), which subsequently dissociates into three stair-rod dislocations (tetrahedron edges, $\boldsymbol{b}$ = a/6<110>), each one of which is accompanied by a Shokley partial ($\boldsymbol{b}$ = a/6<112>) that forms the tetrahedron faces as they expand into the remaining {111} planes. Another explanation for its formation is based on glide of jogged screw dislocations [38]. However, many of the observed tetrahedra are found close to dislocations, where a large number of vacancies may be expected as they climb, but already in dislocation-free regions (*cf.* Fig. 7b), which supports the vacancy collapse hypothesis. Both SF types (tetragonal and nodes) are prevalent in Fig. 7c among additional dislocation loops. While the SF tetrahedra cannot be unequivocally accounted for the high-temperature deformation mechanisms, they relate to the low SF of the SX CrCoNi alloy, and can be associated to gliding dislocations, either directly (see above) or indirectly via a high vacancy concentration being emitted from them. However, as it was found that dislocations are locked onto their glide planes, climb and its vacancy emission probably occur when interacting with strain fields of adjacent dislocations within clusters. In Fig. 7f the dislocation-free regions are colored green, and dislocation clusters marked as dotted green lines. Thus, their mobility is strongly limited by the extended SF and their nucleation may be favored in the already disrupted regions, causing the emergence of a grid structure of clustered dislocations, and dislocation-free areas.

SX CrCoNi shows a low SFE and therefore a high amount of stacking faults at high temperatures. Because of the higher barrier effect of the SF, the material behavior of CrCoNi shows a slower creep deformation compared to SX Cantor alloy. The absence of stacking faults in the SX Cantor alloy thus allows a quicker reconfiguration and recovery of the substructures, leading to larger cells with more dense dislocation cell walls. Cross slip can be seen here as an ease for perfect dislocations to bypass obstacles and be built into cell walls, leaving a larger volume and free path for new dislocations, which is in line with the faster creep rates. On the contrary, the extended dislocations found in the SX CrNiCo alloy become sessile such that they may remain as obstacles for new dislocations. They form part of the cell walls and shorten the path of incoming dislocations that interact with them, *i.e.*, decrease the cell size, making the recovery process slower, and consequently also creep rates.

The positive impact of the SF on the creep properties is visible up to a

temperature of 1100 °C for SX CrCoNi related to the Cantor alloy (Fig. 3).

4. Conclusions

The following statements can be drawn for the mechanical and microstructural characterization of MEA CrCoNi compared to HEA Cantor alloy, both in single crystal and single-phase state:

1. Despite the lower difference in atomic radius of the CrCoNi alloy (δ = 1.6 %), which should lead to lower creep properties compared to SX Cantor alloy (δ = 3.6 %) due to the lower solid solution strengthening effect, SX CrCoNi has a significantly better creep resistance in the temperature range 700 °C – 1100 °C.
2. The configurational entropy ΔS_{conf} is not a dominant factor on creep properties of pure SX Ni (ΔS_{conf} = 0 R), SX CrCoNi (1.1 R), and SX Cantor alloy (1.6 R). The CrCoNi alloy has a lower configurational entropy but higher creep resistance against SX Cantor alloy.
3. The lower SFE of SX CrCoNi (γ_{SFRT} = 22 mJ m^{-2}/55 mJ m^{-2} $\gg$ $\gamma_{SF700°C} \geq$ 27 mJ m^{-2}) is the major influencing factor for the better creep properties compared to SX Cantor alloy (γ_{SFRT} = 30 mJ m^{-2}/ 55 mJ m^{-2} < $\gamma_{SF700°C}$). To reach the same creep rate, a stress level of 108 MPa is necessary for SX CrCoNi in comparison to 80 MPa for SX Cantor alloy. Other influencing factors like oxidation effects, grain size effects, grain boundary sliding, grain boundary diffusion, or precipitate effects are excluded by using single crystal, single phase material and testing in vacuum.
4. SX CrCoNi still has a high amount of stacking faults at 700 °C compared to SX Cantor alloy. Extended dislocation nodes with stacking faults and strong solute interactions act as barriers for the dislocation movement and lead to higher creep resistance. In addition, the stacking faults are associated to a grid structure of dislocation clusters and dislocation-free areas in the CrCoNi alloy.
5. Finally, the driving factor influencing the mechanical properties of the alloys remains with the alloying elements. It becomes evident, that the increased creep resistance of SX CrCoNi is directly linked to the higher content (33.3 at.% instead of 20 at.% for the Cantor alloy) of the elements Cr and Co. The large relative content of these two elements significantly reduces the SFE of the alloy.

Funding

This research work was funded by German Research foundation (DFG) projects GL 181/56 and supported by the priority program SPP2006 “Compositionally Complex Alloys - High Entropy Alloys (CCA-HEA)”. PSO and LAJ acknowledge funding German Research Foundation (DFG) within the Project n°. 398838389. Parts of this work were performed at the electron microscopy center at BAM.

CRediT authorship contribution statement

C. Gadelmeier: Writing – original draft, Visualization, Investigation. **L. Agudo Jácome:** Writing – original draft, Visualization, Resources, Investigation. **P. Suárez Ocaño:** Writing – original draft, Visualization, Investigation. **U. Glatzel:** Writing – review & editing, Supervision, Resources, Funding acquisition, Conceptualization.

Declaration of competing interest

The authors declare that they have no known competing financial interests or personal relationships that could have appeared to influence the work reported in this paper.

Data availability

Data will be made available on request.

References

[1] J.-W. Yeh, S.-K. Chen, S.-J. Lin, J.-Y. Gan, T.-S. Chin, T.-T. Shun, C.-H. Tsau, S.-Y. Chang, Nanostructured high-entropy alloys with multiple principal elements: novel alloy design concepts and outcomes, Adv. Eng. Mater. 6 (2004) 299–303, https://doi.org/10.1002/adem.200300567.
[2] B. Cantor, I.T.H. Chang, P. Knight, A.J.B. Vincent, Microstructural development in equiatomic multicomponent alloys, Mater. Sci. Eng., A 375–377 (2004) 213–218, https://doi.org/10.1016/j.msea.2003.10.257.
[3] B.C. Murty, J.W. Yeh, S. Ranganathan, High-Entropy Alloys, Elsevier, London UK, 2014.
[4] E.P. George, D. Raabe, R.O. Ritchie, High-entropy alloys, Nat. Rev. Mater. 4 (2019) 515–534, https://doi.org/10.1038/s41578-019-0121-4.
[5] D.B. Miracle, O.N. Senkov, A critical review of high entropy alloys and related concepts, Acta Mater. 122 (2017) 448–511, https://doi.org/10.1016/j.actamat.2016.08.081.
[6] C. Gadelmeier, S. Haas, T. Lienig, A. Manzoni, M. Feuerbacher, U. Glatzel, Temperature dependent solid solution strengthening in the high entropy alloy CrMnFeCoNi in single crystalline state, Metals 10 (2020) 1–13, https://doi.org/10.3390/met10111412.
[7] T. Keil, D. Utt, E. Bruder, A. Stukowski, K. Albe, K. Durst, Solid solution hardening in CrMnFeCoNi-based high entropy alloy systems studied by a combinatorial approach, J. Mater. Res. 36 (2021) 2558–2570, https://doi.org/10.1557/s43578-021-00205-6.
[8] J. Rösler, H. Harders, M. Bäker, Mechanisches Verhalten der Werkstoffe, Springer Fachmedien Wiesbaden, Wiesbaden, 2012, https://doi.org/10.1007/978-3-8348-2241-3.
[9] R. Bürgel, H.J. Maier, T. Niendorf, Handbuch Hochtemperatur-Werkstofftechnik, Springer Fachmedien Wiesbaden, Wiesbaden, 2019, https://doi.org/10.1007/978-3-658-25314-1.
[10] C. Barrett, O. Sherby, Influence of stacking fault energy on high temperature creep of pure metals, Trans. Metall. Soc. AIME (1965) 1116–1119.
[11] M.F. Ashby, H.J. Frost, Deformation-mechanism Maps, Pergamon Press., Oxford, 1982.
[12] J.Y. He, C. Zhu, D.Q. Zhou, W.H. Liu, T.G. Nieh, Z.P. Lu, Steady state flow of the FeCoNiCrMn high entropy alloy at elevated temperatures, Intermetallics 55 (2014) 9–14, https://doi.org/10.1016/j.intermet.2014.06.015.
[13] C.B. Carter, S.M. Holmes, The stacking-fault energy of nickel, Philos Mag A J Theor Exp Appl Phys 35 (1977) 172, https://doi.org/10.1080/14786437708232942.
[14] A. Korner, H.P. Karnthaler, Weak-beam study of glide dislocations in h.c.p. cobalt, Philos Mag A Phys Condens Matter, Struct Defects Mech Prop. 48 (1983) 469–477, https://doi.org/10.1080/01418618308234904.
[15] R.E. Schramm, R.P. Reed, Stacking fault energies of fcc fe-Ni alloys by x-ray diffraction line profile analysis, Metall. Trans. A 7 (1976) 359–363, https://doi.org/10.1007/BF02642831.
[16] M.F. De Campos, S.A. Loureiro, D. Rodrigues, M.C.A. Da Silva, N.B. De Lima, Estimative of the stacking fault energy for a FeNi(50/50) Alloy and a 316L stainless steel, in: Mater Sci Forum, 2008, pp. 3–7, https://doi.org/10.4028/www.scientific.net/msf.591-593.3.
[17] G. Laplanche, A. Kostka, C. Reinhart, J. Hunfeld, G. Eggeler, E.P. George, Reasons for the superior mechanical properties of medium-entropy CrCoNi compared to high-entropy CrMnFeCoNi, Acta Mater. 128 (2017) 292–303, https://doi.org/10.1016/j.actamat.2017.02.036.
[18] S.F. Liu, Y. Wu, H.T. Wang, J.Y. He, J.B. Liu, C.X. Chen, X.J. Liu, H. Wang, Z.P. Lu, Stacking fault energy of face-centered-cubic high entropy alloys, Intermetallics 93 (2018) 269–273, https://doi.org/10.1016/j.intermet.2017.10.004.
[19] A.J. Zaddach, C. Niu, C.C. Koch, D.L. Irving, Mechanical properties and stacking fault energies of NiFeCrCoMn high-entropy alloy, JOM 65 (2013) 1780–1789, https://doi.org/10.1007/s11837-013-0771-4.
[20] W. Weißbach, Werkstoffkunde und Werkstoffprüfung, Vieweg+Teubner Verlag, Wiesbaden, 1994, https://doi.org/10.1007/978-3-663-13878-5.
[21] U. Glatzel, F. Schleifer, C. Gadelmeier, F. Krieg, M. Müller, M. Mosbacher, R. Völkl, Quantification of solid solution strengthening and internal stresses through creep testing of Ni-containing single crystals at 980 °C, Metals 11 (2021) 1130, https://doi.org/10.3390/met11071130.
[22] C.M.F. Rae, L. Zhang, Primary creep in single crystal superalloys: some comments on effects of composition and microstructure, Mater. Sci. Technol. 25 (2009) 228–235, https://doi.org/10.1179/174328408X369311.
[23] J.L. Caron, J.W. Sowards, Weldability of nickel-base alloys, in: Compr Mater Process, Elsevier, 2014, pp. 151–179, https://doi.org/10.1016/B978-0-08-096532-1.00615-4.
[24] S. Haas, M. Mosbacher, O. Senkov, M. Feuerbacher, J. Freudenberger, S. Gezgin, R. Völkl, U. Glatzel, Entropy determination of single-phase high entropy alloys with different crystal structures over a wide temperature range, Entropy 20 (2018) 654, https://doi.org/10.3390/e20090654.
[25] C.H. Konrad, M. Brunner, K. Kyrgyzbaev, R. Völkl, U. Glatzel, Determination of heat transfer coefficient and ceramic mold material parameters for alloy IN738LC investment castings, J. Mater. Process. Technol. 211 (2011) 181–186, https://doi.org/10.1016/j.jmatprotec.2010.08.031.
[26] E. Fleischmann, M.K. Miller, E. Affeldt, U. Glatzel, Quantitative experimental determination of the solid solution hardening potential of rhenium, tungsten and molybdenum in single-crystal nickel-based superalloys, Acta Mater. 87 (2015) 350–356, https://doi.org/10.1016/j.actamat.2014.12.011.
[27] G. Laplanche, M. Schneider, F. Scholz, J. Frenzel, G. Eggeler, J. Schreuer, Processing of a single-crystalline CrCoNi medium-entropy alloy and evolution of its

thermal expansion and elastic stiffness coefficients with temperature, Scripta Mater. 177 (2020) 44–48, https://doi.org/10.1016/j.scriptamat.2019.09.020.
[28] D. Redka, C. Gadelmeier, J. Winter, M. Spellauge, C. Eulenkamp, P. Calta, U. Glatzel, J. Minár, H.P. Huber, Sub-picosecond single-pulse laser ablation of the CrMnFeCoNi high entropy alloy and comparison to stainless steel AISI 304, Appl. Surf. Sci. 544 (2021) 148839, https://doi.org/10.1016/j.apsusc.2020.148839.
[29] A.G. Mora-García, M. Mosbacher, J. Hastreiter, R. Völkl, U. Glatzel, J. Muñoz-Saldaña, Creep behavior of polycrystalline and single crystal Ni-based superalloys coated with Ta-containing NiCoCrAlY by high-velocity oxy-fuel spraying, Scripta Mater. 178 (2020), https://doi.org/10.1016/j.scriptamat.2019.12.023, 552–526.
[30] M. Laurent-Brocq, A. Akhatova, L. Perrière, S. Chebini, X. Sauvage, E. Leroy, Y. Champion, Insights into the phase diagram of the CrMnFeCoNi high entropy alloy, Acta Mater. 88 (2015) 355–365, https://doi.org/10.1016/j.actamat.2015.01.068.
[31] S. Guo, C. Ng, J. Lu, C.T. Liu, Effect of valence electron concentration on stability of fcc or bcc phase in high entropy alloys, J. Appl. Phys. 109 (2011) 103505, https://doi.org/10.1063/1.3587228.
[32] Y.C. Huang, C.H. Su, S.K. Wu, C. Lin, A study on the hall-petch relationship and grain growth kinetics in FCC-structured high/medium entropy alloys, Entropy 21 (2019), https://doi.org/10.3390/e21030297.
[33] F. Otto, A. Dlouhý, K.G. Pradeep, M. Kubĕnová, D. Raabe, G. Eggeler, E.P. George, Decomposition of the single-phase high-entropy alloy CrMnFeCoNi after prolonged anneals at intermediate temperatures, Acta Mater. 112 (2016) 40–52, https://doi.org/10.1016/j.actamat.2016.04.005.
[34] K. Hagihara, Effect of short-range order on the high-temperature plastic deformation behavior of Ni–Cr–W, Ni–W, and Ni–Re single crystals, J. Mater. Sci. Technol. 165 (2023) 143–152, https://doi.org/10.1016/j.jmst.2023.04.058.
[35] F. Otto, A. Dlouhý, C. Somsen, H. Bei, G. Eggeler, E.P. George, The influences of temperature and microstructure on the tensile properties of a CoCrFeMnNi high-entropy alloy, Acta Mater. 61 (2013) 5743–5755, https://doi.org/10.1016/j.actamat.2013.06.018.
[36] G. Gottstein, Materialwissenschaft und Werkstofftechnik, Springer Berlin Heidelberg, Berlin, Heidelberg, 2014, https://doi.org/10.1007/978-3-642-36603-1.
[37] K.-Y. Tsai, M.-H. Tsai, J.-W. Yeh, Sluggish diffusion in Co–Cr–Fe–Mn–Ni high-entropy alloys, Acta Mater. 61 (2013) 4887–4897, https://doi.org/10.1016/j.actamat.2013.04.058.
[38] P.M. Anderson, J.P. Hirth, J. Lothe, Theory of Dislocations, Third Edition, 2017.
[39] E. Curtet, B. Kedjar, F. Mompiou, H. Bahsoun, F. Pailloux, A. Courcelle, M. Bono, P. Olier, L. Thilly, Loss of ductility in optimized austenitic steel at moderate temperature: a multi-scale study of deformation mechanisms, Materialia 9 (2020) 100562, https://doi.org/10.1016/j.mtla.2019.100562.
[40] N. Thompson, Dislocation nodes in face-centred cubic lattices, Proc. Phys. Soc. B 66 (1953) 481–492, https://doi.org/10.1088/0370-1301/66/6/304.
[41] P.C.J. Gallagher, The influence of alloying, temperature, and related effects on the stacking fault energy, Metall. Trans. A 19 (1) (1970) 2429–2461, https://doi.org/10.1007/BF03038370, 1970.
[42] Hideji Suzuki, Segregation of solute atoms to stacking faults, J Phys Soc Japan. 17 (1962) 322–325.
[43] D. Hull, D.J. Bacon, Introduction to Dislocations, Elsevier Ltd, 2011, https://doi.org/10.1016/C2009-0-64358-0.